Simple analytical models and analysis of bistable vibration energy harvesters

Adrien Morel, Ludovic Charleux, Quentin Demouron, Aya Benhemou, David Gibus, Camille Saint-Martin, Aurélien Carré, Émile Roux, Thomas Huguet, Adrien Badel

Simple analytical models and analysis of bistable vibration energy harvesters

Adrien Morel[1], Ludovic Charleux[1], Quentin Demouron[1], Aya Benhemou[1], David Gibus[1], Camille Saint-Martin[1], Aurélien Carré[1], Émile Roux[1], Thomas Huguet[2], Adrien Badel[1]

[1] SYMME, Université Savoie Mont-Blanc, France [2] LAPLACE, Université de Toulouse, France

E-mail: adrien.morel@univ-smb.fr
Received xxxxxx
Accepted for publication xxxxxx
Published xxxxxx

Abstract

In order to scavenge the energy of ambient vibrations, bistable vibration energy harvesters constitute a promising solution due to their large frequency bandwidth. Because of their complex dynamics, simple models that easily explain and predict the behavior of such harvesters are missing from the literature. To tackle this issue, this paper derives simple analytical closed-form models of the characteristics of bistable energy harvesters (e.g., power-frequency response, displacement response, cut-off frequency of the interwell motion) by mean of truncated harmonic balance methods. Measurements on a bistable piezoelectric energy harvester illustrate that the proposed analytical models allow the prediction of the mechanical displacement and harvested power, with a relative error below 10%. From these models, the influences of various parameters such as the inertial mass, the acceleration amplitude, the electromechanical coupling, and the resistive load, are derived, analyzed and discussed. The proposed models and analysis give an intuitive understanding of the dynamics of bistable vibration energy harvesters, and can be exploited for their design and optimization.

Keywords: Energy harvesting, Nonlinear dynamics, Harmonic balance, Analytical model, Bi-stability, Vibrations.

1. Introduction

Energy harvesting has been widely investigated in order to design autonomous communicating electronic systems that can be powered by the energy present in their surroundings. This energy can be available under many different forms: solar radiations [1], thermal gradients [2], mechanical vibrations [3], electromagnetic waves [4], … The present study focuses on vibration energy harvesters (VEH).

During the last decades, several types of VEH have been investigated by the research community [5]. Linear VEH made of a linear oscillator and an electromechanical transducer (e.g., a piezoelectric material or a moving magnet in a coil) show interesting performances when the vibration frequency matches the resonant frequency of the linear oscillator. However, a slight mismatch of the vibration frequency with the resonant frequency of the oscillator drastically decreases the harvested power [6]. This constitutes a major issue in many environments, where the vibration spectrum might vary with time. Furthermore, other factors such as aging and temperature variations can also induce such mismatch, which considerably hinders the long-term performances of linear VEH [7]. In order to increase the frequency bandwidth of VEH, part of the research community focused on the study and design of nonlinear oscillators, and more particularly on bistable VEH [8]. While bistable VEH might exhibit relatively large frequency bandwidths [9], the understanding of their complex dynamics is still thoroughly studied as a topical issue [10-12]. Indeed, unlike linear VEH whose model allows to analytically explore their dynamics and develop physical intuition, nonlinear VEH remain, in most cases, studied with numerical simulations which might hinder physical insights. Therefore, simple analytical models providing meaningful explanations of the behavior of bistable VEH are lacking in the literature. The aim of this paper is to derive simplified closed-form expressions that accurately model the behavior of bistable VEH, and to exploit these expressions to study the impacts and influence of the parameters of bistable VEH on their dynamics.

As illustrated in Fig.1, the study of bistable VEH started around 2008 with the works of Shahruz [13] and McInnes et al. [14]. In their seminal article, Gammaitonni's group studied

numerically and experimentally a bistable energy harvester under random vibrations [15, 16]. In the next years, many numerical and experimental studies of bistable VEH flourished in the literature [17-19]. For instance, Erturk et al. studied (numerically and experimentally) the broadband behavior of a piezomagnetoelectric bistable VEH under harmonic excitations [17]. Two years later, Erturk and Inman numerically and experimentally studied the high-energy orbits of bistable VEH, proving that the bistable VEH can generate an order of magnitude larger harvested power compared to linear VEH, at several vibration frequencies [18].

While the vast majority of bistable VEH analysis (including the aforementioned ones [13-19]) were purely numerical and experimental, Stanton et al. proposed to apply analytical methods to predict the behavior of bistable VEH [20], as depicted in Fig.1. By mean of the harmonic balance, they predicted key features of bistable VEH, and proved the existence of an optimal impedance load and electromechanical coupling in order to maximize the harvested power. Thereafter, other analytical approaches such as the multiple scales method have been applied to study the influence of the electromechanical coupling, load, and potential function on the VEH characteristics [21]. Recently, Liu et al. [22] followed by Huguet et al. [23] semi-analytically studied (with the harmonic balance) the influences of the stiffness, mass, coupling, load resistance, and buckling level on the power-frequency response of bistable VEH. Yet, all the aforementioned analyses [20-23], while analytical, do not allow to derive the closed-form expressions of the characteristics of the bistable VEH (e.g., its power-frequency response, or its cut-off frequency) as a function of its parameters.

In order to understand the influences of the bistable VEH parameters on its characteristics, the present paper derives new closed-form models of the two types of forced response than can be obtained with bistable VEH: interwell and intrawell motions. From these models, closed-form expressions of the displacement and power in interwell and intrawell motions, as well as the cut-off frequency of the interwell motion are obtained. As illustrated in Fig.1 and Table 1, the proposed expressions constitute the first step toward a simple closed-form description of bistable VEH dynamics. These expressions allow to develop an intuitive understanding of the influences of the bistable VEH parameters, just as it has already been done for linear VEH [24] and monostable nonlinear VEH [25].

The proposed study is decomposed as follows: the second section establishes the analytical model of the bistable energy harvester, based on the study of its intrawell and interwell motions. The equations governing the displacement amplitude, the harvested power, the interwell cut-off frequency, and the relations between electrically induced damping and resistive load are derived. The third section introduces the numerical and experimental validation of the analytical models, by mean of a piezoelectric VEH prototype. The fourth section exploits the proposed analytical models to study how each parameter of the harvester (e.g., the inertial mass, the electromechanical coupling, or the quality factor of the resonator) impacts its displacement amplitude, cut-off frequency, and power-frequency response.

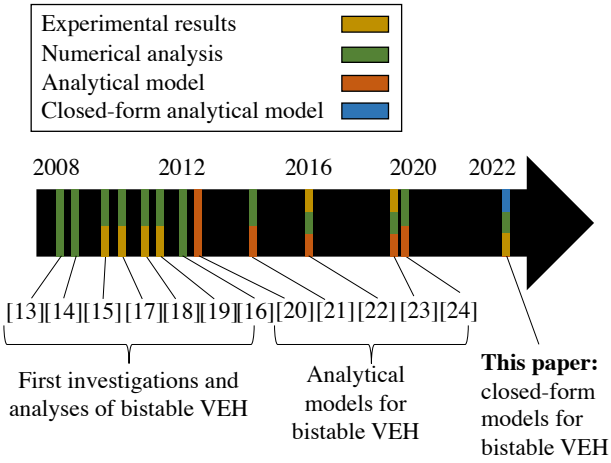

Figure 1. Brief history of the development of models for bistable VEH: from numerical analysis to closed-form models.

Table 1. Contribution of this article compared to previous literature on analysis and modeling of bistable VEH.

References		[26]	[22]	[23]	[27]	**This Paper**
Year		'14	'17	'19	'22	'22
Type of behaviors	Harmonic	✓	✓	✓	✓	✓
	Sub-harmonic	✗	✗	✓	✓	✗
	Chaos	✗	✗	✗	✓	✗
Method of study	Exp.	✗	✓	✓	✗	✓
	Num.	✓	✓	✓	✓	✓
	Analytical	✗	✓	✓	✗	✓
	Analytical + closed-form expressions	✗	✗	✗	✗	✓
Closed-form model of the displacement		✗	✗	✗	✗	✓
Closed-form model of the harvested power		✗	✗	✗	✗	✓

2. Electromechanical model of bistable VEH

This section reminds the electromechanical model of bistable VEH, and summarizes the assumptions made in the present paper. Thereafter, analytical expressions of the displacement and power in intrawell and interwell motions are derived. Finally, the relation between electrically-induced damping and resistive load is discussed.

2.1 Electromechanical harvester dynamics

A bistable VEH is made of a nonlinear bistable mechanical resonator. Part of the mechanical energy of the resonator is converted in electrical energy by mean of an electromechanical transducer. While the structure of the mechanical resonator, the origin of the bistable behavior (e.g, with magnets or with buckled beams), and the choice of the electromechanical transducer (e.g., piezoelectric or electromagnetic transducer) have been widely investigated in the literature, the equation modeling the motion of the nonlinear resonator remains, in most cases, identical. Using the normalization proposed in [22], the equation expressing the motion of the mass of any symmetrical bistable resonator is given by (1),

$$\gamma(t) = \ddot{x} + \frac{\omega_0^2}{2}\left(\frac{x^2}{x_0^2} - 1\right) x + \frac{\omega_0}{Q}\dot{x} + f(x, \dot{x}, v, i) \qquad (1)$$

with x being the displacement of the mass M. ω_0 and Q correspond to the natural angular frequency and mechanical quality factor of the equivalent linear harvester[1], respectively. $+x_0$ and $-x_0$ correspond to the two stable positions of the mass. f is a function that models the influence of the electrical interface on the mass motion, due to the electromechanical transduction. γ is the acceleration of the ambient vibration.

Figure 2 shows the mass-spring-damper model equivalent to (1). Note that the stiffness K_{nl} of the model shown in Fig.2 is nonlinear in order to take into account the cubic nonlinearity of (1).

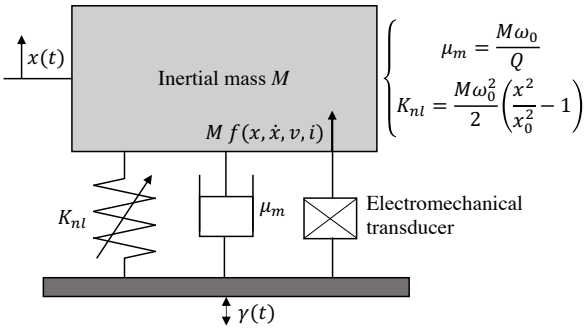

Figure 2. Lumped element model of a generic bistable energy harvester modeled by (1).

The mechanical energy in the bistable resonator E_{mech} can be obtained by integrating (1) times M in the case of an unforced regime ($\gamma = 0$) with no damping ($\omega_0/Q = 0$) and no electrical influence ($f(x, \dot{x}, v, i) = 0$).

$$E_{mech} = M \int \left[\ddot{x} + \frac{\omega_0^2}{2}\left(\frac{x^2}{x_0^2} - 1\right) x\right] dx$$
$$E_{mech} = \frac{\dot{x}^2}{2} M + \frac{M\omega_0^2}{4} x^2 \left[\frac{x^2}{2x_0^2} - 1\right] \qquad (2)$$

Figure 3.a shows the evolution of this mechanical energy as a function of the mass displacement x and the mass speed $\dot{x}$. The double-well potential is characteristic of a bistable resonator, with two stable positions ($x = \pm x_0$) and one instable position ($x = 0$). Figure 3.b shows the iso-energies lines of the bistable VEH in the phase space $(x, \dot{x})$.

One possible limit-cycle of (1) is the oscillation of the mass around one of the two stable equilibria of the harvester. Such limit-cycle is denoted as *intrawell motion* in Fig. 3.b. Another possible limit-cycle of (1) is the oscillation of the mass around the two stable equilibria of the harvester. Such limit-cycle is denoted as *interwell motion* in Fig. 3.b.

As illustrated in Fig. 3.b, intrawell motion usually results in a small-amplitude displacement that leads to poor harvesting performances. On the other hand, interwell motion usually results in relatively large amplitude displacement and harvested power. This limit-cycle is considered favorable, and many approaches have been developed in the literature in order to jump to this orbit from other, less favorable, orbits.

[1] The equivalent linear harvester is obtained for small oscillations of the bistable VEH around one of its stable position, x_0.

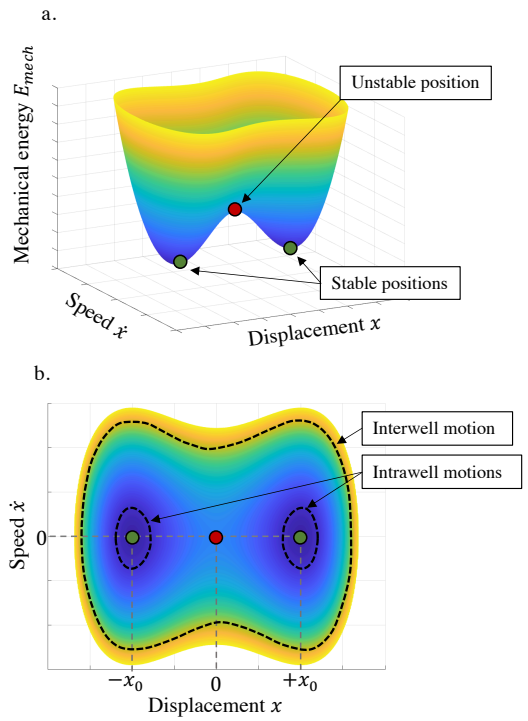

Figure 3. a. Double-well potential and b. iso-energies in the phase-space of a bistable resonator.

2.2 Assumptions and limitations of the models

In this paper, we will consider the following assumptions:
i) The acceleration of the ambient vibration γ is mono-harmonic and can be written $\gamma(t) = \gamma_m \cos(\omega t + \psi)$, with γ_m its amplitude, ω its angular frequency and ψ its phase. This assumption can be considered reasonable as long as most of the vibrational energy is concentrated around a single vibration frequency, which is the case in various applications [28, 29].
ii) The impact of the electrical interface on the mass motion can be taken into account as a damper μ_e called *electrical damper*. This assumption is always true in the case of electromagnetic energy harvesters, and is reasonable for piezoelectric energy harvesters (PEH), as long as the electromechanical coupling of the harvester remains relatively weak ($k^2 < 0.2$).
iii) The mechanical displacement is considered to be sinusoidal, either around one of the two stable equilibria (intrawell motion) or around the two stable equilibria (interwell motion). This assumption is reasonable since the harmonics of the mechanical displacement in interwell motion remain relatively low [30]. Such assumption will be confirmed by the measured waveforms in section 3.2.

Under the two first assumptions, (1) can be rewritten as (3),

$$\gamma_m \cos(\omega t + \psi) = \ddot{x} + \frac{\omega_0^2}{2}\left(\frac{x^2}{x_0^2} - 1\right) x + \frac{\omega_0(1+\beta)}{Q}\dot{x} \quad (3)$$

With $\beta = \frac{\mu_e}{\mu_m}$ being the ratio of the electrical damper μ_e on the mechanical damper μ_m. Except when specified otherwise, the examples given in this paper are taken with the set of parameters shown in Table 2.

Table 2. Model parameters used in the numerical simulations. The VEH parameters are the same than the prototype used in the experimental validation (section 3).

Variable	Quantity (unit)	Value
M	Inertial mass (g)	6.5
x_0	Stable position (mm)	0.8
ω_0	Linear natural angular frequency (rad.s^{-1})	333
R	Resistive load (Ohm)	1000
Q	Mechanical quality factor	80

Note that the analyses derived in this paper, because of their simplicity, have some limitations:

i) Because of the nature of the truncated harmonic balance method used in this paper, the proposed models do not allow to predict chaos and sub-harmonic behaviors.
ii) The proposed models are valid if the bistable VEH is modeled by a Duffing equation. This is generally true as long as the buckling-level of the VEH remains relatively small.
iii) The proposed models are valid in case of sinusoidal excitations. Therefore, such model can only be used in applications where the vibrations are mainly sinusoidal (e.g., to harvest energy from rails [28] or from motor engines [29]).

As long as the aforementioned assumptions and limitations are taken into account, the proposed models allow to accurately predict the behavior of bistable VEH, as illustrated in section 3 of the present paper.

2.3 Intrawell motion

As shown in Fig.3.b, intrawell motion can be modelled as a small-amplitude oscillation around one of the two equilibrium positions. In this case, the mass displacement can be expressed as (4),

$$x = \pm x_0 + \tilde{x} \quad (4)$$

with $\tilde{x} \ll x_0$ being the small-amplitude oscillation of the mass. Combining (3) with (4) and removing the high-order terms yields (5).

$$\gamma_m \cos(\omega t + \psi) = \ddot{\tilde{x}} + \tilde{x}\,\omega_0^2 + \frac{\omega_0(1+\beta)}{Q}\dot{\tilde{x}} \quad (5)$$

For intrawell motion, (5) shows that the harvester behaves as a linear VEH whose natural angular frequency is ω_0 and equivalent mechanical quality factor is Q. From (5), the expression of the amplitude of the displacement can be given by:

$$\tilde{x}_m = \frac{\gamma_m}{\sqrt{(\omega_0^2 - \omega^2)^2 + \left(\frac{\omega_0 \omega}{Q}(1+\beta)\right)^2}} \quad (6)$$

The harvested power can then be calculated from the power dissipated in the electrical damper μ_e:

$$P_{intra} = \dot{\tilde{x}}^2 \, \mu_e = \frac{1}{2Q} \frac{\omega^2 \, \gamma_m^2 \, \beta \, M \, \omega_0}{(\omega_0^2 - \omega^2)^2 + \left(\frac{\omega_0 \omega}{Q}(1+\beta)\right)^2} \quad (7)$$

2.4 Displacement amplitude in interwell motion

In order to approximate the trajectory of the bistable harvester in the phase-space $(x, \dot{x})$ in case of interwell motion, we study the iso-energies drawn in Fig.4.b[2]. Choosing the initial condition $(x_m, 0)$, the initial mechanical energy in the mass is given by $E_{mech} = \frac{M\omega_0^2}{4} x_m^2 \left[\frac{x_m^2}{2x_0^2} - 1\right]$. Since the mechanical energy is conserved on any iso-energy orbit, the expression of the mass speed can be obtained from (2).

$$\dot{x} = \frac{dx}{dt} = \frac{\omega_0 \, x_m}{x_0} \sqrt{\frac{1}{2}\left[\frac{x_m^2}{2} - \frac{x^4}{2x_m^2} + \frac{x^2 x_0^2}{x_m^2} - x_0^2\right]} \quad (8)$$

Isolating dt in (8) and integrating it on a period of vibration yields the duration of the period T taken by the system to realize a single orbit.

$$T = \int_0^T dt = \frac{4 \, x_0}{x_m \omega_0} \int_0^{x_m} \frac{dx}{\sqrt{\frac{1}{2}\left[\frac{x_m^2}{2} - \frac{x^4}{2x_m^2} + \frac{x^2 x_0^2}{x_m^2} - x_0^2\right]}} \quad (9)$$

Therefore, from (9), it is possible to obtain the expression of the relation between the angular frequency of the harvester ω and the amplitude of the displacement x_m.

$$\omega = \frac{x_m \omega_0 \pi}{2 \, x_0} \left[\int_0^{x_m} \frac{dx}{\sqrt{\frac{1}{2}\left[\frac{x_m^2}{2} - \frac{x^4}{2x_m^2} + \frac{x^2 x_0^2}{x_m^2} - x_0^2\right]}} \right]^{-1} \quad (10)$$

The integral in (10) does not have any explicit solution, but can be solved numerically to obtain the relation between the angular frequency ω and the amplitude of the displacement x_m. Figure 4 shows that x_m increases with ω which agrees with the literature on the subject [31], and is in good agreement with the exact solution obtained by integrating (1) numerically (yellow and grey dashed lines in Fig.4). Note that the relation between the normalized amplitude of interwell motion and the normalized frequency is valid for any bistable energy harvester whose dynamics is described by (1). Indeed, both (10) and the numerical solution obtained by integrating (1) remain (almost) unchanged for any choice of the harvester parameters (e.g., for any acceleration amplitude γ_m or any mechanical quality factor Q, provided $Q > 20$ and $\gamma_m < x_0 \omega_0^2$).

Another possibility to obtain a simple expression of the displacement amplitude of interwell motion is to assume that the displacement is sinusoidal $x(t) = x_m \cos(\omega t)$.

Replacing this expression in (3) and applying the harmonic balance method to the first-order terms leads to (11).

$$\begin{cases} -\omega^2 x_m - \frac{x_m \omega_0^2}{2} + \frac{3\omega^2}{8x_0^2} x_m^3 = \gamma_m \cos(\psi) \\ \frac{\omega_0(1+\beta)}{Q} \omega x_m = \gamma_m \sin(\psi) \end{cases} \quad (11)$$

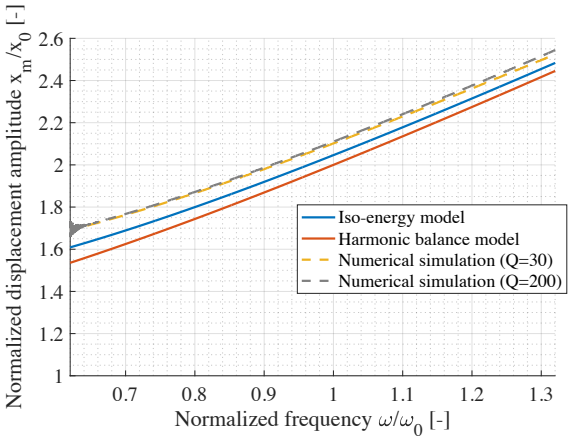

Figure 4. Normalized displacement amplitude x_m/x_0 of interwell motion of the bistable harvester as a function of the normalized frequency ω/ω_0. The results have been obtained with the iso-energy method (10) (blue line) and with the harmonic balance method (red line). The numerical results have been obtained by solving (1), with $\gamma_m = 10 m/s^2$ and $\beta = 0$.

[2] By doing so, we assume that the trajectories followed by the bistable harvester remain almost the same as when considering no damping and no excitation. This assumption is reasonable as long as $Q > 20$ and $\gamma_m < x_0 \omega_0^2$.

Squaring and adding the two equations of (11) yields (12).

$$0 = \left(-1 - \frac{\omega_0^2}{2\omega^2} + \frac{3x_m^2}{8x_0^2}\right)^2 + \left(\frac{\omega_0(1+\beta)}{Q\omega}\right)^2 - \left(\frac{\gamma_m}{x_m\omega^2}\right)^2 \quad (12)$$

The analytical expression of x_m can be obtained from (12), but its expression is cumbersome and does not yield further insights. However, a much simpler expression can be obtained by making a few assumptions. Considering the relatively large quality factor of most harvesters ($Q\omega \gg \omega_0(1+\beta)$), and, because in interwell motion, the mass acceleration amplitude ($x_m\omega^2$) is usually much larger than the vibration acceleration (γ_m), the two last terms of (12) are, in most cases, negligible compared to the first one.

This mean that the displacement amplitude x_m can be estimated from a simplified equation given by (13).

$$0 = \left(-\omega^2 - \frac{\omega_0^2}{2} + \frac{3\omega^2}{8x_0^2}x_m^2\right)^2 \quad (13)$$

Solving (13) leads to an analytical expression of interwell motion displacement amplitude:

$$x_m = \frac{2}{\sqrt{3}}x_0\sqrt{1+\frac{2\omega^2}{\omega_0^2}} \quad (14)$$

As shown in Fig.4, this expression is also in good agreement with the semi-analytical results given by (10) and the solutions obtained by integrating (1) numerically (relative error < 15% for low ω/ω_0 and < 5% for large ω/ω_0). An interesting insight that can be observed from (14) is that x_m does not depend, in first approximation, on the quality factor of the harvester nor on the acceleration amplitude. The numerical simulations in Fig.4 confirm that the displacement amplitude of the harvester in interwell motion does not depend much on Q and γ_m. This constitutes a fundamental difference with the behavior of linear harvesters (or the behavior of the intrawell motion) whose displacement amplitude is proportional to the acceleration amplitude [24].

Linear VEH exhibit a single resonant frequency that does not vary with the displacement amplitude, but the displacement amplitude of linear VEH (at resonance) can take any value depending on the acceleration amplitude. On the other hand, the interwell motion of bistable VEH corresponds to a resonance whose characteristics are slightly different from the resonance of linear VEH. The resonant frequency of bistable VEH can take multiple value, depending on the displacement amplitude. However, the interwell motion displacement amplitude of bistable VEH (for a given vibration frequency) can only take a single value and does not vary with the acceleration amplitude.

2.5 Limits of existence of interwell motion

As broadly described in the literature, there exists a cut-off angular frequency ω_c from where the interwell motion stops existing. As reported in [32] and in the appendix A of this paper, ω_c always occur with a phase lag of 90° between the displacement $x(t)$ and the input vibration $\gamma(t)$. Replacing $\psi = 90°$ in (11) leads to (15).

$$\begin{cases} -\omega_c^2 x_m - \dfrac{x_m\omega_0^2}{2} + \dfrac{3\omega_c^2}{8x_0^2}x_m^3 = 0 \\ \dfrac{\omega_0(1+\beta)}{Q}\omega_c x_m = \gamma_m \end{cases} \quad (15)$$

From (15) yields the expressions of the displacement amplitude $x_m|_{\omega=\omega_c}$, and the expression of ω_c.

$$\begin{cases} x_m|_{\omega=\omega_c} = \dfrac{2}{\sqrt{3}}x_0\sqrt{1+\dfrac{2\omega_c^2}{\omega_0^2}} \\ \omega_c = \dfrac{\omega_0}{2}\sqrt{\left[-1+\sqrt{1+\dfrac{6Q^2\gamma_m^2}{\omega_0^4 x_0^2(\beta+1)^2}}\right]} \end{cases} \quad (16)$$

If $2\omega_c^2 \gg \omega_0^2$, (16) can be further simplified:

$$\begin{cases} x_m|_{\omega=\omega_c} \approx \dfrac{2\sqrt{2}}{\sqrt{3}}x_0\dfrac{\omega_c}{\omega_0} \\ \omega_c \approx \dfrac{1}{2}\sqrt{\dfrac{\sqrt{6}Q\gamma_m}{x_0(\beta+1)}} \end{cases} \quad (17)$$

(16) and (17) reveal important information on intrawell motion of bistable VEH. (17) shows that the cut-off angular frequency does not depend much of the value of ω_0, meaning that there is no direct link between the resonant frequency of the intrawell motion and the cut-off frequency of interwell motion. The second equation of (16) proves that the quality factor of the harvester Q and the acceleration amplitude γ_m share the same influence on the cut-off angular frequency of interwell motion. Indeed, a larger Q and/or γ_m tend to increase ω_c. On the other hand, a larger stable position x_0 tends to decrease ω_c while increasing the displacement amplitude $x_m|_{\omega=\omega_c}$. This can be understood from Fig.3: a greater x_0 tends to increase the size of interwell orbits. However, the energy lost in the mechanical (and electrical) damper(s) tend to increase with the size of the orbit. The cut-off frequency of interwell motion decreases with a larger damping, which explains why a larger x_0 tends to decrease ω_c. Finally, a greater β also tends to decrease ω_c. Indeed, a greater β implies a larger electrical damping that can be seen as a reduction of the quality factor of the harvester. This last influence means that the value of the resistive load (or the choice of the

electrical interface) has a non-negligible impact on the interwell motion cut-off frequency.

2.6 Harvested power in interwell motion

The harvested power P_{harv} is the power dissipated in the electrical damper. The expression of the harvested power is given by (18) (assuming that the displacement is sinusoidal).

$$P_{harv} = \frac{1}{T}\int_0^T \mu_e \dot{x}^2 \, dt = \frac{M \, \omega_0 \, \beta \, \omega^2 x_m^2}{2Q} \tag{18}$$

Combining (18) with (14), the expression of the harvested power in interwell motion can be estimated.

$$P_{harv} = \frac{2 \, M \, \omega_0 \, \beta \, \omega^2 x_0^2}{3Q}\left(1 + \frac{2\omega^2}{\omega_0^2}\right) \tag{19}$$

Figure 5 shows the evolution of the harvested power with three different acceleration amplitudes as a function of the vibration frequency. Figure 5 proves that the expression of the harvested power in interwell motion (19) is in good agreement with numerical simulations for the three values of the acceleration amplitude (forward frequency sweeps). When the interwell motion stops existing (e.g., for $\omega/\omega_0 \in [2.2,2.6]$), the harvester operates in intrawell motion. In this case, the simulated harvested power is in good agreement with the expression of the harvested power in intrawell motion (7). Note that (16) predicts that the cut-off angular frequency of intrawell motion ω_c is equal to $1.16\omega_0$, $1.38\omega_0$and $1.66\omega_0$when the acceleration amplitude γ_m is 7m.s^{-2}, 10m.s^{-2}, and 15m.s^{-2}, respectively. These predictions are in good agreement (relative error below 5%) with the numerical simulation shown in Fig.5.

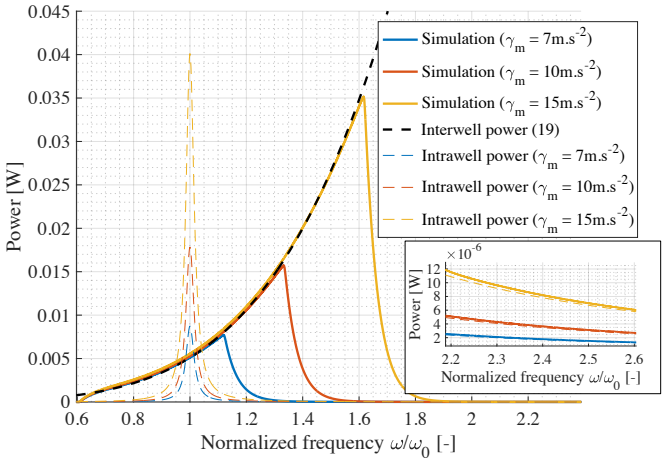

Figure 5. Simulation of the harvested power for $\gamma_m = 7m.s^{-2}$ (blue), $\gamma_m = 10m.s^{-2}$ (red), $\gamma_m = 15m.s^{-2}$ (yellow), and theoretical predictions for interwell motion (black dashed line) and intrawell motion (colored dashed lines).

From (17) and (18), the expression of the harvested power at the cut-off frequency, $P_{harv}|_{\omega=\omega_c}$, can also be expressed. Since both ω and x_m reach their maximum value when $\omega = \omega_c$ (because for higher ω, the interwell motion stops existing), $P_{harv}|_{\omega=\omega_c}$ corresponds to the maximum harvested power (for a given electrical damping) as a function of the vibration frequency.

$$P_{harv}|_{\omega=\omega_c} = \frac{M \, Q \, \gamma_m^2 \, \beta}{2 \, \omega_0 \, (\beta+1)^2} \tag{20}$$

$P_{harv}|_{\omega=\omega_c}$ is maximized when $\beta = 1$, meaning that the electrical damping is equal to the mechanical damping. In this case, the harvested power is equal to the well-known power limit of any linear VEH P_{lim} [7] [33].

$$\max(P_{harv}|_{\omega=\omega_c}) = \frac{M \, Q \, \gamma_m^2}{8 \, \omega_0} = P_{lim} \tag{21}$$

(21) is in agreement with [24] that proves that the power limit of nonlinear energy harvester is the same than the power limit of the equivalent linear VEH (i.e., a linear VEH sharing the same mass M, the same ω_0 and the same Q than the bistable VEH). Figure 6 illustrates that the damping ratio maximizing the power $P_{harv}|_{\omega=\omega_c}$ is $\beta = 1$, and that, in this case, $P_{harv}|_{\omega=\omega_c} = P_{lim}$. Furthermore, Fig.6 shows that the bandwidth of the harvester can be increased by mean of a fine tuning of β (e.g., with a tunable electrical interface that optimizes the electrical damping such as in [34] and [35]). Increasing β allows to decrease ω_c and to maximize the harvested power for lower frequencies (because, for a given β, the power is maximized for $\omega = \omega_c$). On the other hand, decreasing β allows to increase ω_c and to maximize the harvested power for higher frequencies.

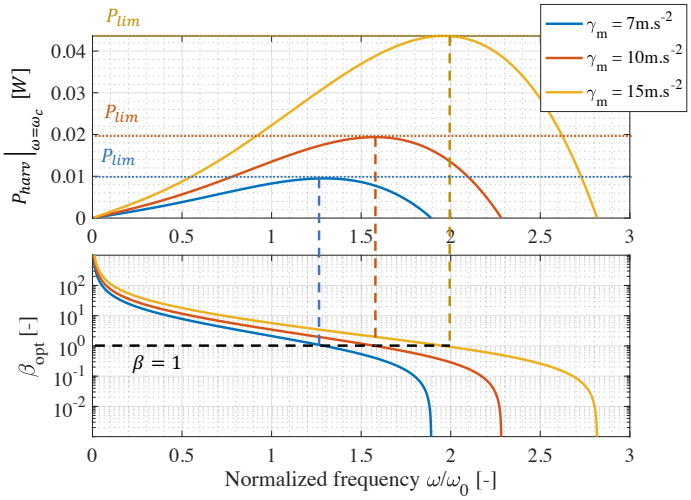

Figure 6. Power that can be obtained with a fine tuning of the damping ratio β, and optimal damping ratio β_{opt} maximizing the harvested power a function of the normalized frequency. The results have been obtained for three acceleration amplitudes: $\gamma_m = 7m.s^{-2}$ (blue), $\gamma_m = 10m.s^{-2}$ (red) and $\gamma_m = 15m.s^{-2}$ (yellow).

2.7 Relationship between β and interface resistance R

The relation between the damping ratio β and the electrical interface connected to the bistable energy harvester (e.g., a resistive load) largely depends on the type of bistable energy harvester and on the definition of $f(x,\dot{x},v,i)$ in (1). The following subsections derive the relations between β and R for two types of piezoelectric energy harvesters. Note that these analyses can easily be extended to electromagnetic VEH because of the duality of piezoelectric/electromagnetic energy harvesters [36].

a) PEH with linear influence of the voltage

If the influence of the electrical interface on the harvester dynamics is linear, the equations modeling the electromechanical behavior of the harvester are given by (22). As a matter of example, this is the case of bistable PEH whose bistability is induced with repulsive magnets (Fig.7).

$$\begin{cases} \gamma(t) = \ddot{x} + \dfrac{\omega_0^2}{2}\left(\dfrac{x^2}{x_0^2} - 1\right) x + \dfrac{\omega_0}{Q}\dot{x} + \dfrac{\alpha v_p}{M} \\ \alpha\dot{x} = C_p\dot{v_p} + \dfrac{v_p}{R} \end{cases} \quad (22)$$

Where α is the force factor, v_p is the voltage across the piezoelectric material, and C_p is the clamped capacitance of the piezoelectric element.

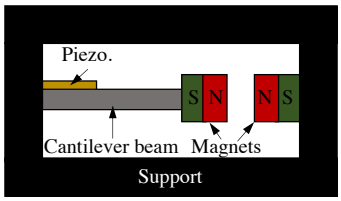

Figure 7. Example of bistable PEH where the piezoelectric voltage acts linearly on the harvester dynamics. The piezoelectric material is fixed on a cantilever beam, and bistability is induced with two repulsive magnets.

As shown in (22), the impact of the voltage on the VEH dynamics is linear: a force proportional to v_p is electrically induced. From the second equation of (22) in the frequency domain yields the expression of $\underline{v_p}$ given by (23).

$$\underline{v_p} = \underline{x}\,\frac{\alpha}{C_p}\left(\frac{r^2\Omega^2}{1+r^2\Omega^2} + j\,\frac{r\Omega}{1+r^2\Omega^2}\right) \quad (23)$$

Where $r = R\,C_p\,\omega_0$ is the normalized resistive load, and $\Omega = \omega/\omega_0$ is the normalized frequency. The imaginary part of $\underline{v_p}$ (in other words, the quadrature part of the piezoelectric voltage) is the one contributing to the electrical damping [7]. From the first equation of (22) and (23), the expression of β_{lin} can be found:

$$\beta_{lin} = \frac{\alpha^2}{\mu_m\,C_p\,\omega}\,\frac{r\Omega}{1+r^2\Omega^2} = k_m^2\,Q\,\frac{r}{1+r^2\Omega^2} \quad (24)$$

With $k_m^2 = \alpha^2/(KC_p)$ the squared electromechanical coupling of the PEH. As shown in (24), a stronger electromechanical coupling leads to a larger electrical damping. The maximum value that can be taken by β_{lin} is given by (25).

$$\mathrm{Max}(\beta_{lin}) = \frac{k_m^2 Q}{2\Omega} \quad (25)$$

Note that the normalized resistance maximizing β_{lin} is $r = 1/\Omega$ ($R = 1/(C_p\omega)$), which is the exact same result than with a linear PEH [24, 37].

b) PEH with nonlinear influence of the voltage

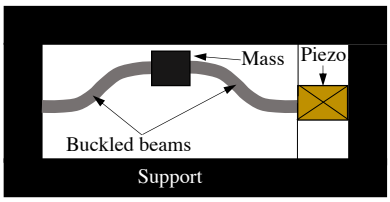

Figure 8. Example of bistable PEH where the piezoelectric voltage acts nonlinearly on the harvester dynamics. The piezoelectric energy harvester is a buckled beam structure. The piezoelectric material is fixed between one of the buckled beam and the support.

If the influence of the electrical interface on the VEH dynamics is nonlinear, the equations modeling the electromechanical behavior of the VEH are given by (26). As a matter of example, this is the case of a bistable PEH whose bistability is induced with buckled beams. As detailed in [23] and illustrated in Fig.8, the piezoelectric material is located on the side of the mechanical resonator. Note that the piezoelectric material could also be placed along the moving beams, as detailed in [38].

$$\begin{cases} \gamma(t) = \ddot{x} + \dfrac{\omega_0^2}{2}\left(\dfrac{x^2}{x_0^2} - 1\right) x + \dfrac{\omega_0}{Q}\dot{x} + \dfrac{2\alpha\,x\,v_p}{M\,L} \\ \dfrac{2\alpha\dot{x}x}{L} = C_p\dot{v_p} + \dfrac{v_p}{R} \end{cases} \quad (26)$$

In (26), L represents the distance between the inertial mass and the frame [23]. The second equation of (26) is nonlinear, because of the term $2\alpha\dot{x}x/L$. Contrarily to (22), the impact of the voltage on the bistable dynamics is nonlinear and is also proportional to x. In order to find the value of β, one can find the expression of the piezoelectric voltage by applying the harmonic balance to the first order terms of the second equation of (26).

$$\begin{cases} v_p(t) = a_V \cos(2\omega t) + b_V \sin(2\omega t) \\ a_V = \dfrac{2\alpha}{LC_p} x_m^2 \dfrac{r^2\Omega^2}{1+4r^2\Omega^2} \\ b_v = -\dfrac{\alpha}{LC_p} x_m^2 \dfrac{r\Omega}{1+4r^2\Omega^2} \end{cases} \quad (27)$$

Note that the frequency of the voltage v_p is two times larger than the vibration frequency. Indeed, when the voltage reaches an extremum, the piezoelectric material reaches a maximum of compression, meaning that the period of the voltage is equal to half-period of the mass displacement. Combining the first expression of (26) with (27) and with the first-harmonic expression of x ($x(t) = x_m \cos(\omega t)$), then removing the high-order terms, yields the expression of the electrically-induced force:

$$F_p = \frac{2\alpha\, x\, v_p}{L} \approx \frac{2\alpha x_m}{L}\left(\frac{a_v \cos(\omega t)}{2} + \frac{b_v \sin(\omega t)}{2}\right) \quad (28)$$

The out-of-phase term of this force F_p with the mechanical displacement x contributes to the damping of the harvester. Therefore, the expression of the electrical damping can be obtained from (27) and (28):

$$\mu_e = \frac{\alpha^2}{\omega\, C_p L^2} \frac{x_m^2}{\omega} \frac{r\Omega}{1+4r^2\Omega^2} \quad (29)$$

From (29) yields the expression of the damping ratio[3], β_{nlin}:

$$\beta_{nlin} = \frac{k_m^2 Q}{4} \frac{x_m^2}{x_0^2} \frac{r}{1+4r^2\Omega^2} \quad (30)$$

The damping ratio in case of a nonlinear piezoelectric force is also proportional to $k_m^2 Q$, similarly as in the linear case (24). However, the damping ratio in the nonlinear case also depends on $\left(\frac{x_m^2}{x_0^2}\right)$, meaning that a larger displacement amplitude leads to a larger effective electromechanical coupling. The maximum value that can be taken by β_{nlin} is given by (31) and is obtained when $r = \frac{1}{2\Omega}$ ($R = \frac{1}{2C_p\omega}$).

$$\mathrm{Max}(\beta_{nlin}) = \frac{k_m^2 Q}{16\Omega}\left(\frac{x_m}{x_0}\right)^2 = \mathrm{Max}(\beta_{lin})\left(\frac{x_m}{2\sqrt{2}x_0}\right)^2 \quad (31)$$

$\mathrm{Max}(\beta_{nlin})$ is greater than $\mathrm{Max}(\beta_{lin})$ if $x_m > 2\sqrt{2}\, x_0$. This means that structures such as the one introduced in Fig.8 might be more efficient that the ones presented in Fig.7 if the acceleration amplitude (and displacement amplitude) is important enough.

3. Numerical and experimental validation

3.1 Experimental setup and bistable prototype

In order to validate the proposed model, a prototype of bistable PEH has been developed, based on the structure shown in Fig.8 (piezoelectric energy harvester with buckled beams). The prototype is shown in Fig.9, and its dimensions are summarized in Table 3. The beams as well as the inertial mass are made in steel, while the amplified piezoelectric actuator (APA) is made with PZT and is the APA120S fabricated by Cedrat Technologies.

Table 3. Dimensions of the proposed PEH prototype.

Variable	Quantity (unit)	Identified Value
M_{bb}	Mass of a buckled beam (g)	0.1
l_{bb}	Length of a buckled beam (mm)	35
w_{bb}	Width of a buckled beam (mm)	10
t_{bb}	Thickness of a buckled beam (mm)	0.2
M_m	Mass of the inertial mass (g)	6.5
l_m	Length of the inertial mass (mm)	13
w_m	Width of the inertial mass (mm)	10
t_m	Thickness of the inertial mass (mm)	11

The parameters of this harvester have been identified under weak sinusoidal excitation ($\gamma_m = 0.05m.s^{-2}$) and are summarized in Table 4.

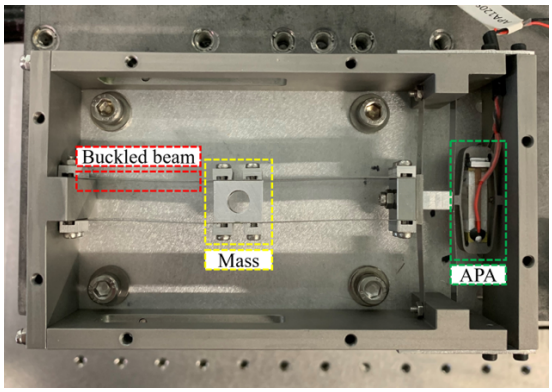

Figure 9. Prototype of bistable PEH based on a buckled beam structure.

[3] Note that the expressions of β_{lin} and β_{nlin} are only valid if the excitation is sinusoidal.

Table 4. Identified parameters of the bistable energy harvester prototype.

Variable	Quantity (unit)	Identified Value
M	Total inertial mass (g)	6.5
L	Horizontal distance from the mass to the frame (mm)	35
l	Length of a buckled beam (mm)	35.01
x_0	Stable position (mm)	0.8
ω_0	Linearized natural angular frequency (rad.s^{-1})	333
C_p	Piezoelectric capacitance (μF)	1.12
Q	Quality factor of the resonator	80
α	Force factor (N.V^{-1})	0.16
k_m^2	Expedient electromechanical coupling	0.068

As detailed in [23], the parameters of the bistable PEH shown in Fig.9 can be expressed as follows:

$$\begin{cases} \omega_0 = \dfrac{x_0}{L}\sqrt{\dfrac{4K}{M}} \\ Q = \dfrac{x_0}{L}\dfrac{\sqrt{4KM}}{\mu_m} \\ x_0 = \sqrt{l^2 - L^2} \\ k_m^2 = \dfrac{\alpha^2}{K\,C_p} \\ k^2 = \dfrac{k_m^2}{1 + k_m^2} \end{cases} \quad (32)$$

With K being the stiffness of the APA (approximately 0.342 N/μm), and l being the length of a buckled beam.

Experimental measurements have been conducted with the setup shown in Fig.10. The prototype (Fig.9) is fixed on an electromagnetic shaker driven by a power amplifier. The acceleration of the shaker is sensed with an accelerometer and is sent to the dSpace board. As shown in Fig.10, the same dSpace board sends a signal to the power amplifier driving the shaker. By mean of a PI controller, the amplitude of the shaker acceleration is maintained to $\gamma_m = 5m.s^{-2}$ throughout the whole experiment. The electrodes of the piezoelectric transducer are connected to a programmable resistor whose value is adjusted with another signal coming from the dSpace board. The voltage across the piezoelectric element is sent to the dSpace board through a voltage follower. The speed and displacement waveforms are also sensed with a laser vibrometer.

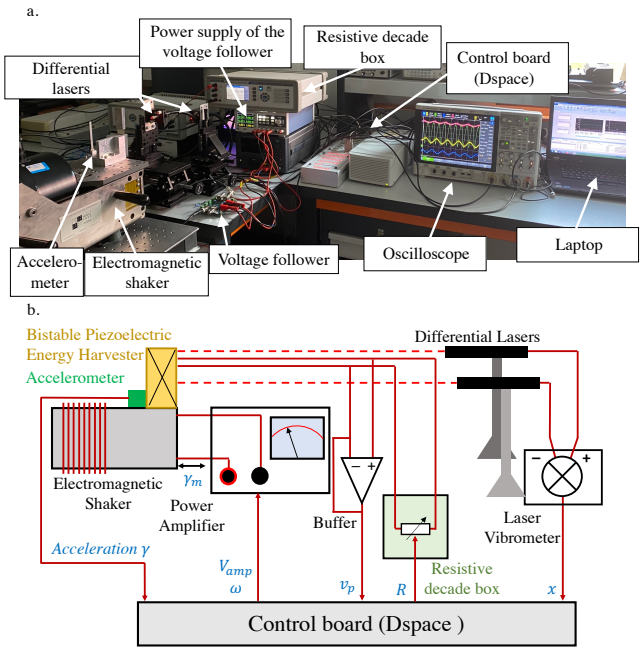

Figure 10. a. Experimental setup used to validate the proposed models of bistable energy harvesters and b. Schematic of this setup.

3.2 Experimental results

Before each run, the amplitude of the sinusoidal acceleration is increased to $\gamma_m = 18m.s^{-2}$ in order to jump from intrawell to interwell orbits. Thereafter, the acceleration amplitude is gradually decreased to $\gamma_m = 5m.s^{-2}$. Additional information on the experimental procedure is provided in Appendix B.

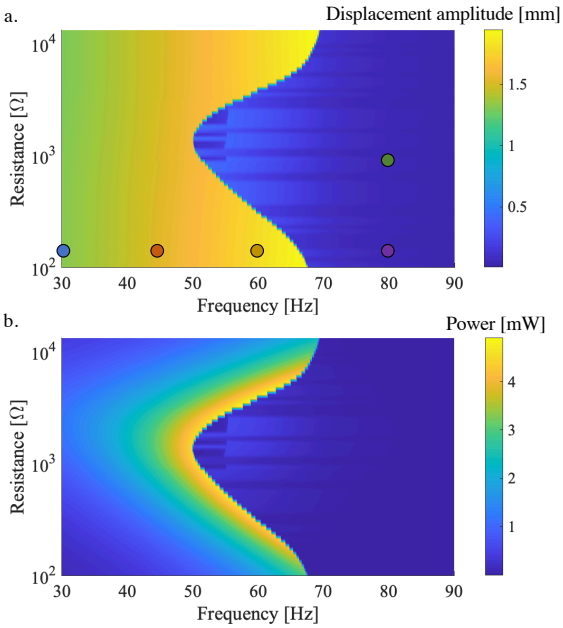

Figure 11. Experimental measurements of a. displacement amplitude and b. harvested power as a function of the vibration frequency and the resistance of the load, for $\gamma_m = 5m.s^{-2}$. Each dot corresponds to a waveform and phase portrait in Fig.12.

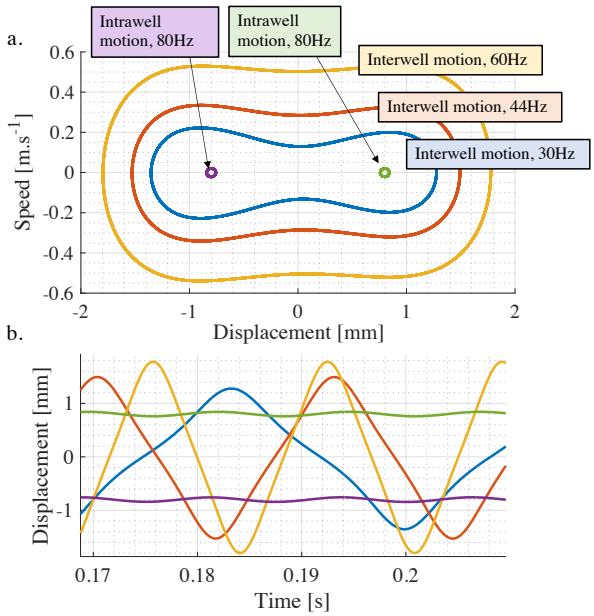

Figure 12. Experimental measurements of a. intrawell and interwell phase portraits and b. time signals.

The voltage, displacement, speed and acceleration waveforms are then measured for 600 frequencies between 30Hz and 90Hz. The same procedure is repeated for 70 resistances from 100Ω to $30k\Omega$. Figure 11 shows the displacement amplitude x_m and the harvested power P_{harv} (calculated from the squared root mean square value of the voltage divided by the resistance) as a function of the vibration frequency and the resistance of the load. As shown in Fig.11, the displacement amplitude and power are large in the left part of the plane (for low vibration frequencies). Indeed, for these frequencies, interwell motion occurs, leading to large displacement amplitudes. For higher frequencies, intrawell motion occurs, which explains why the displacement amplitude as well as the harvested power are much lower. Note that interwell motion cut-off frequency depends on the resistance value R, and hence on the damping ratio β, which is consistent with the theoretical prediction (16). This point will be further detailed in the next subsection.

Figure 12.a shows examples of intrawell and interwell phase portraits, with various frequencies and resistances (each one of them corresponding to a dot in Fig.11.a). These phase portraits illustrate that interwell and intrawell motions are relatively close to the iso-energy orbits shown in Fig.3.b, and are consistent with other publications on bistable energy harvesters [27].

Figure 12.b illustrates the time-varying mechanical displacement that can be associated with each phase portrait. The purple and green waveforms illustrate intrawell motion of the inertial mass, around one of the two well ($\pm 0.8mm$) of the PEH. The blue, red and yellow waveforms illustrate interwell motion of the inertial mass for vibration frequencies of 30Hz, 45Hz and 60Hz, respectively. As shown in Fig.11.a, the displacement amplitude slightly increases with the vibration frequency. Note that interwell and intrawell motions remain relatively close to sinusoidal motion (with total harmonic distortion below 0.1) which supports the first-harmonic assumption discussed in section 2.4.

3.3 Experimental validation of the proposed models

Figure 13.a shows the experimental measurements, the simulation, and the theoretical prediction of the displacement amplitude as a function of the vibration frequency. The experimental results are in good agreement with the model, the relative error on the displacement in interwell motion remaining below 10%. As predicted from (14), the interwell motion displacement amplitude (for a fixed vibration frequency) does not vary much (less than 2% variation) with the resistance R.

Figure 13 also shows that for $R = 1.3k\Omega$ (yellow curves), the interwell motion cut-off frequency is around 50Hz. For a larger resistance $R = 5.7k\Omega$ (red curves), the cut-off frequency becomes 66Hz. This illustrates that the cut-off frequency of the interwell motion depends on the value of the resistance R, which is consistent with the theoretical predictions. Indeed, (30) proves that the resistance R has an impact on the damping ratio β. (16) illustrates that a larger β leads to a lower cut-off frequency.

Figure 13.b shows the harvested power as a function of the vibration frequency. Again, the experimental, theoretical and simulated results are in good agreement, with a relative difference always below 15%. As predicted by the theory, the power (in interwell motion) grows with the vibration frequency. When the cut-off frequency is reached, the harvested power drops from a few mW to a few hundreds of µW. While the displacement amplitude (for a given vibration frequency) does not vary much with the resistance value, the power largely depends on the choice of the resistance. For example, for a vibration frequency of 50Hz, the power reaches 4.4mW with $R = 1.3k\Omega$, 2.2mW with $R = 5.7k\Omega$, and 1mW with $R = 139\Omega$. For all these resistances, the displacement amplitude x_m remains almost equal to 1.6mm.

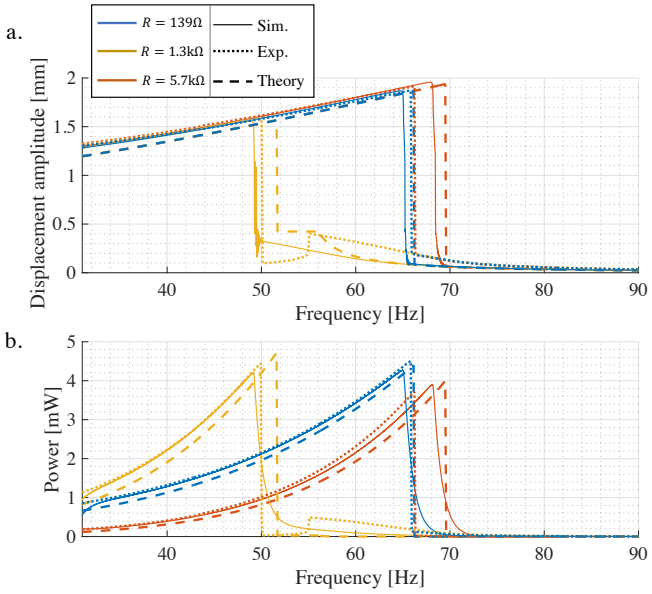

Figure 13. Experimental measurements (dashed lines), simulation (dotted lines), and theoretical prediction (solid lines) of a. displacement amplitude and b. harvested power, for three resistances.

The evolution of the cut-off frequency as a function of the resistance value can be observed in Fig.14.a. As predicted in section 2.7, there exists a resistance value ($\approx 1.4k\Omega$) that maximizes the damping ratio β and thus minimizes the cut-off frequency (50Hz). The value of this resistance is in agreement with the theory which predicts that the resistance value maximizing β is given by $R = \frac{1}{2C_p\omega} = 1.42k\Omega$. As shown in Fig.14.a, when the resistance gets larger or smaller than this particular value, the cut-off frequency of the harvester becomes larger, up to 70Hz. Indeed, with a larger (or smaller) resistance, the value of the damping ratio β decreases, which increases the cut-off frequency (16). The experimental results illustrated in Fig.14.a are in good agreement with the theoretical predictions, with a relative error below 10%. One may note that the error of the model is maximal for extreme values of the resistance ($R > 7k\Omega$ or $R < 200\Omega$). Indeed, for these resistances, the mechanical displacement at the cut-off frequency becomes larger than 1.8mm (Fig.11). Under such large displacement, the mechanical quality factor of the harvester tends to decrease, which reduces the cut-off frequency of the harvester (16). The variation of the mechanical quality factor (due to nonlinear behavior of mechanical losses) has not been taken into account in our model, but could be added in the future, in order to obtain closer predictions for extreme values of the resistance.

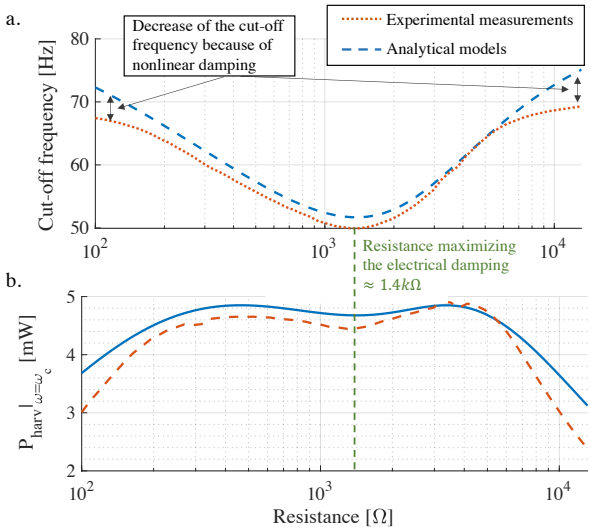

Figure 14. a. Cut-off frequency and b. harvested power at the cut-off frequency $P_{harv}|_{\omega=\omega_c}$ as a function of the resistance.

Figure 14.b. shows the harvested power at the cut-off frequency as a function of the resistance. One may notice that the resistance maximizing the damping ratio is not the one maximizing the harvested power. Indeed, in order to maximize the harvested power, the damping ratio should be equal to 1 (in other words, the electrical damping should be equal to the mechanical damping), as predicted by (20) and (21). Since the electromechanical coupling of our prototype is relatively large, the maximum value of β is larger than 1. Therefore, the resistance maximizing β ($\approx 1.4k\Omega$) overdamps the harvester, and does not maximize the harvested power. The resistances maximizing the harvested power ($\approx$ 4.8mW) are, theoretically, around 450Ω and $4k\Omega$. Experimentally, one may notice that the second resistance ($4k\Omega$) allows to harvest a slightly larger power than the first one (450Ω).

The bifurcation of the optimal resistances with strong coupling harvesters is a common feature of linear piezoelectric energy harvesters, and has already been thoroughly studied in the literature [24,39].

Figure 14 illustrates the trade-off in the choice of the resistance value for bistable energy harvesters. Indeed, selecting a resistance around $4k\Omega$ allows to harvest a large power of 4.8mW around 60Hz. On the other hand, selecting a $10k\Omega$ resistance decreases the maximum power to 3mW, but increases the cut-off frequency to 69Hz. Therefore, adapting the resistance value (or the input resistance of any electrical interface) according to the vibration frequency with maximum power point tracking (MPPT) algorithms could be particularly useful in order to maximize the harvested power on large frequency bands, and fully exploit the potential of bistable VEH.

3.4 Experimental validation of acceleration amplitude impact

Additional measurements have been realized on the prototype shown in Fig.9, in order to study the effects of the acceleration amplitude on bistable energy harvester dynamics. During these experimentations, the voltage, displacement, speed and acceleration waveforms have been measured for 600 frequencies between 30Hz and 90Hz and for 20 accelerations amplitudes between 2m.s^{-2} and 7m.s^{-2}. The value of the resistance has been arbitrarily fixed to 200Ω.

Figure 15.a shows the experimental measurements, the simulation, and the theoretical prediction of the displacement amplitude as a function of the vibration frequency for three acceleration amplitudes. As predicted from (14) and from Fig.5, the displacement amplitude in interwell motion (for a given vibration frequency) does not vary much (less than 2% variation) with the acceleration amplitude γ_m. The cut-off frequency of the interwell motion, on the other hand, strongly depends on the acceleration amplitude. For an acceleration amplitude of 3.05m.s^{-2}, the cut-off frequency is measured to be 50Hz. When the acceleration amplitude is increased to 4.37 m.s^{-2} and 5.68m.s^{-2}, the cut-off frequency becomes equal to 60Hz and 66Hz, respectively. The relative difference between the experimental cut-off frequency and the theoretical cut-off frequency predicted by (16) remains below 5%, which illustrates the good agreement between the proposed model and the experimental measurements.

The harvested power as a function of the vibration frequency is shown in Fig.15.b. The maximum power increases with the acceleration amplitude, from 1.6mW for $\gamma_m = 3.05m.s^{-2}$ to 5.1mW for $\gamma_m = 5.68m.s^{-2}$. Once again, the experimental data are in good agreement with the theoretical power, with an error below 0.5mW. Figure 15.b confirms the theoretical prediction (20) that the harvested power at the cut-off frequency increases with the square of the acceleration amplitude.

The evolution of the cut-off frequency and $P_{harv}|_{\omega=\omega_c}$ for acceleration amplitudes between 2.2m.s^{-2} and 6m.s^{-2} is illustrated in Fig.16. As predicted by (16) and (21), both the cut-off frequency ($\propto \sqrt{\gamma_m}$) and the harvested power ($\propto \gamma_m^2$) increase with a larger acceleration amplitude. The differences between experimental measurements and analytical models remain below 10% for values of γ_m smaller than 5m.s^{-2}. However, for larger acceleration amplitude, the error of the analytical model becomes more important (67Hz instead of 71Hz and 5.5mW instead of 6.5mW for $\gamma_m = 6\text{m.s}^{-2}$). Similarly as in Fig.14, this error comes from the variation of the mechanical quality factor of the PEH due to mechanical nonlinearities under large mechanical displacements (when x_m >1.8mm).

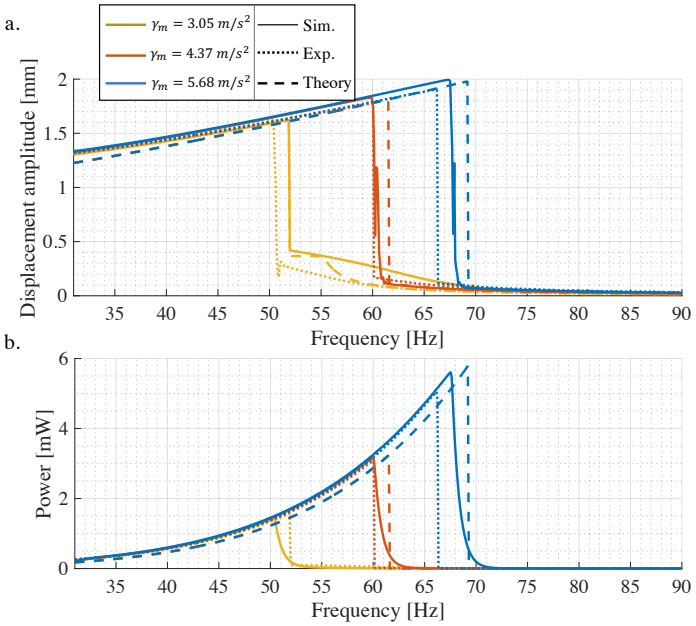

Figure 15. Experimental measurements (dashed lines), simulation (dotted lines), and theoretical prediction (solid lines) of a. displacement amplitude and b. harvested power, for three acceleration amplitudes.

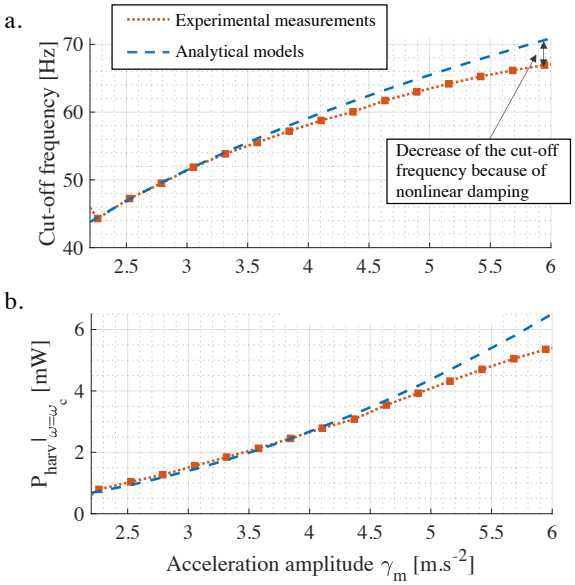

Figure 16. a. Cut-off frequency and b. harvested power at the cut-off frequency $P_{harv}|_{\omega=\omega_c}$ as a function of the acceleration amplitude.

4. An intuitive appreciation of bistable VEH dynamics

The analytical model introduced in this paper allows to understand how the parameters of bistable VEH impact their performances. This section describes and summarizes these impacts in order to provide an intuitive understanding of the interwell behavior. Note that the analyses in sections 4.1-4.5 correspond to the bistable VEH of Fig. 8.

4.1 Impact of x_0

Figure 17 shows the evolution of the displacement amplitude and harvested power as a function of the vibration frequency, for three values of x_0. As predicted by (14), a larger x_0 leads to a larger displacement amplitude. On the other hand, a larger x_0 tends to decrease the cut-off frequency of the interwell motion, as predicted by (16) and (17). As expressed by (18), a larger x_0 leads to a larger harvested power at a given frequency. Nevertheless, Fig. 17 shows that the power at the cut-off frequency $P_{harv}|_{\omega=\omega_c}$ decreases with x_0. As shown in (20), $P_{harv}|_{\omega=\omega_c}$ depends on the damping ratio β which decreases as (x_m/x_0) is reduced (30). Note that the power at the cut-off frequency could also be increased with x_0, if the resistance value was different. Indeed, the relation between $P_{harv}|_{\omega=\omega_c}$ and β is not monotonic. If $\beta > 1$, a larger x_0 would reduce its value and make it closer to its optimal value, $\beta = 1$, increasing $P_{harv}|_{\omega=\omega_c}$. On the other hand, if $\beta < 1$ (as this is the case in Fig.17), a larger x_0 decreases $P_{harv}|_{\omega=\omega_c}$.

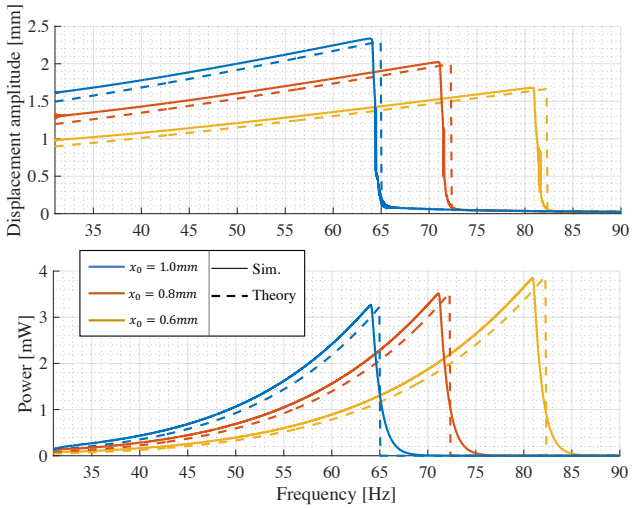

Figure 17. Displacement amplitude and harvested power as a function of the vibration frequency, for various values of x_0, with $R = 100\Omega$ and $\gamma_m = 5m.s^{-2}$ (the other parameter values are given in Table 2).

4.2 Impact of ω_0

Figure 18 shows the evolution of the displacement amplitude and harvested power as a function of the vibration frequency, for three values of ω_0. As shown by the analytical expression of x_m (14), a larger ω_0 leads to a lower displacement amplitude. As predicted by (17), the value of ω_0 has little to no impact on the cut-off frequency of the interwell motion. Since $x_m \propto 1/\omega_0$ (14) and $\beta \propto 1/\omega_0$ (30) (under the assumption that $\omega^2 \gg \omega_0^2$), then $P_{harv} \propto 1/\omega_0^2$ and $P_{harv}|_{\omega=\omega_c} \propto 1/\omega_0^2$. This explains why the power decreases with a larger ω_0 in Fig.18.

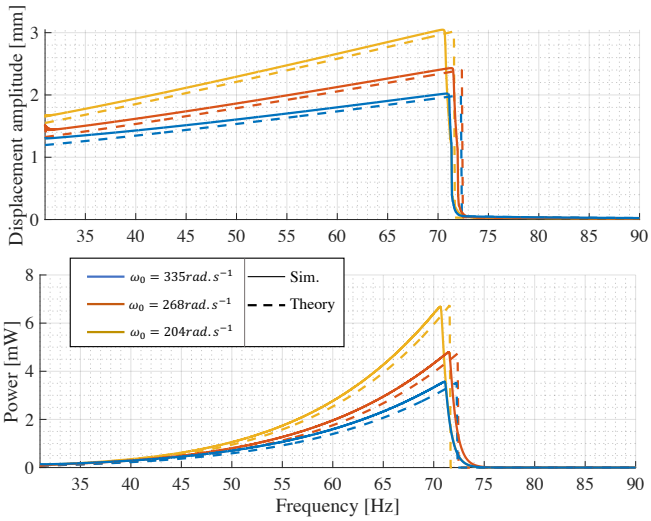

Figure 18. Displacement amplitude and harvested power as a function of the vibration frequency, for various values of ω_0, with $R = 100\Omega$ and $\gamma_m = 5m.s^{-2}$ (the other parameter values are given in Table 2).

4.3 Impact of Q

Figure 19 illustrates that neither the displacement amplitude nor the harvested power depends on the value of Q, for a given vibration frequency. Indeed, as shown by (14), the analytical expression of x_m does not depend on Q. Furthermore, since $\beta \propto Q$, the expression of the harvested power given by (18) proves that P_{harv} does not vary with Q. Nevertheless, as illustrated in Fig.19 and proved by (16), the cut-off frequency of interwell motion gets larger with Q. It can also be noted that the damping ratio β (30) is proportional to Q.

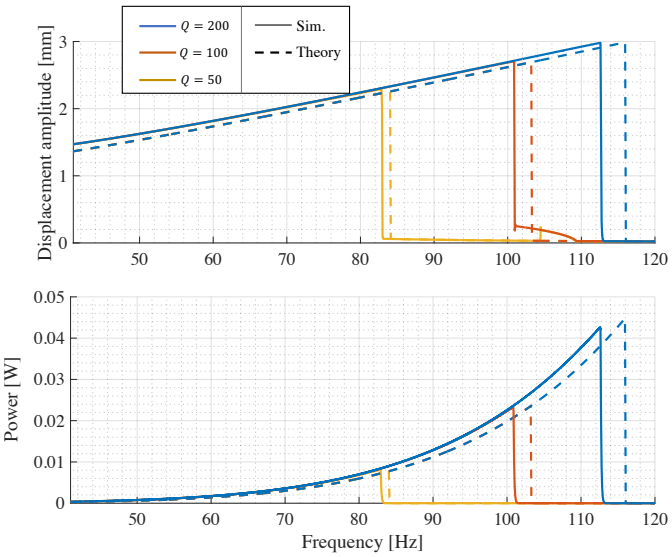

Figure 19. Displacement amplitude and harvested power as a function of the vibration frequency, for various values of Q, with $R = 100\Omega$ and $\gamma_m = 10m.s^{-2}$ (the other parameter values are given in Table 2).

4.4 Impact of M

Figure 20 depicts the evolution of the displacement amplitude and harvested power as a function of the vibration frequency, for three values of the inertial mass, M. Interestingly, the displacement amplitude as well as the interwell cut-off frequency do not depend on M (which is consistent with the analytical expressions (14) and (16)). Conversely, the harvested power is proportional to M, as illustrated by Fig.20 and (18).

4.5 Impact of k_m^2

Figure 21 shows the evolution of the displacement amplitude and harvested power as a function of the vibration frequency, for three values of the electromechanical coupling k_m^2. As predicted by (14), the displacement amplitude does not vary with the value of the electromechanical coupling. Figure 21 also illustrates that the cut-off frequency of the interwell motion becomes smaller with a larger coupling.

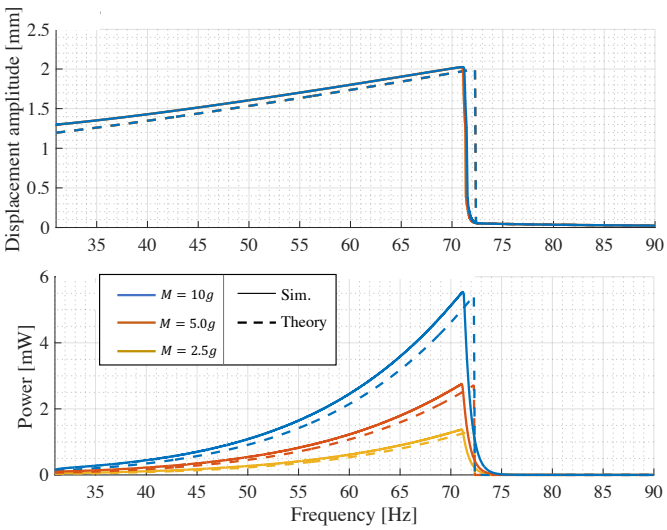

Figure 20. Displacement amplitude and harvested power as a function of the vibration frequency, for various values of M, with $R = 100\Omega$ and $\gamma_m = 5m.s^{-2}$ (the other parameter values are given in Table 2).

Indeed, a stronger coupling implies a larger damping ratio β (30), and therefore a decrease of the cut-off frequency value (16). Because of the increase of the damping ratio β, the harvested power at a given frequency P_{harv} gets larger with a stronger coupling ($P_{harv} \propto \beta$ (19)). Yet, the impact of k_m^2 on the harvested power at the cut-off frequency $P_{harv}|_{\omega=\omega_c}$ is not monotonic, as proven by (21). $P_{harv}|_{\omega=\omega_c}$ is maximized for $\beta = 1$, so if $\beta < 1$, increasing the coupling will increase the power (because β will get closer to its optimal value). If $\beta > 1$, increasing the coupling will decrease the power (because β will get farther from its optimal value) because the harvester will be overdamped by the electrical interface. Such case can be observed in Fig.21. When k_m^2 is equal to 0.05, the value of the power at the cut-off frequency $P_{harv}|_{\omega=\omega_c}$ is 4.55mW (with simulations, red solid line). When k_m^2 is equal to 0.2, the value of the power at the cut-off frequency $P_{harv}|_{\omega=\omega_c}$ is 3.95mW (with simulations, blue solid line). Therefore, in this case, a larger coupling leads to a lower power because of the overdamping phenomenon ($\beta > 1$).

Note that if the input resistance of the electrical interface were adjusted and optimized with an MPPT algorithm (as in [34]), the conclusions of this section would be quite different. Indeed, as shown in section 2.7, tuning the input resistance of the electrical interface allows to tune the damping ratio β. This means that the optimal value of β (β =1) could be reached for any electromechanical coupling k_m^2, as long as the maximum value of β is greater than 1 (31). Furthermore, the maximum value of β depends on k_m^2 (31), which means that a stronger electromechanical coupling leads to a larger range of damping ratio that can be obtained with a tunable electrical interface.

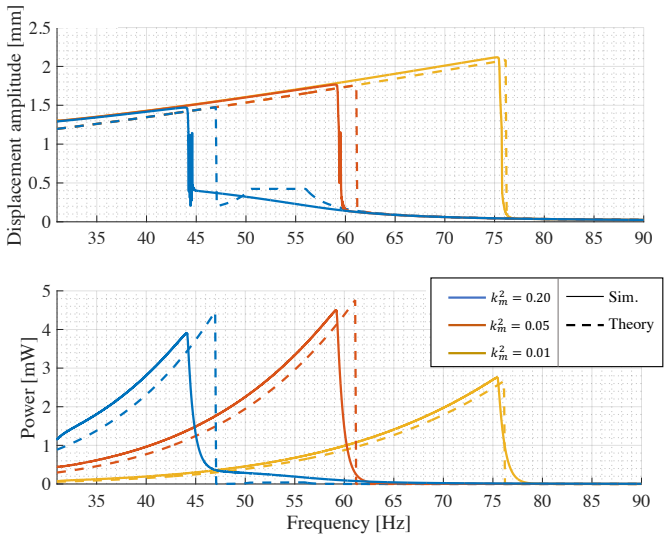

Figure 21. Displacement amplitude and harvested power as a function of the vibration frequency, for various values of k_m^2, with $R = 500\Omega$ and $\gamma_m = 5m.s^{-2}$ (the other parameter values are given in Table 2).

4.6 Summary of the influences in bistable VEH

Table 4 summarizes the impacts of the harvester parameters (M, x_0, ω_0, R, k_m^2, Q, γ_m) on the characteristics of the harvester (x_m, ω_c, β_{max}, P_{harv}, $P_{harv}|_{\omega=\omega_c}$, P_{lim}). Note that the impacts of the vibration acceleration and resistance are depicted in Fig.15 and Fig.13, respectively.

Table 5. Influences of each parameter on various characteristics of the harvester in case of nonlinear influence of the electrical interface (Fig.8). A green color means that an increase of the parameter (left column) increases the considered characteristic. A red color means that an increase of the parameter (left column) decreases the considered characteristic. A yellow color means that the considered characteristic does not vary much with variations of the parameter. A blue color means that the dependency of the characteristic to the parameter is not monotonic. The case where (*) is indicated is valid under the assumption $\omega > \omega_0$. For $\omega < \omega_0$, the case (*) should be green.

Param.	Energy harvester characteristics					
	$x_m(\omega)$	ω_c	β_{max}	$P_{harv}(\omega)$	$P_{harv}\|_{\omega=\omega_c}$	P_{lim}
M	=	=	=	↗	↗	↗
x_0	↗	↘	↘	↗	∿	=
ω_0	↘	=*	↘	↘	↘	↘
R	=	∿	=	∿	∿	=
k_m^2	=	↘	↗	↗	∿	=
Q	=	↗	↗	=	↗	↗
γ_m	=	↗	=	=	↗	↗

Table 6. Influences of each parameter on various characteristics of the harvester in case of linear influence of the electrical interface (Fig.7). A green color means that an increase of the parameter (left column) increases the considered characteristic. A red color means that an increase of the parameter (left column) decreases the considered characteristic. A yellow color means that the considered characteristic does not vary much with variations of the parameter. A blue color means that the dependency of the characteristic to the parameter is not monotonic. The cases where (*) is indicated are valid under the assumption $\omega > \omega_0$. For $\omega < \omega_0$, the cases (*) should be red.

Param.	Influences					
	$x_m(\omega)$	ω_c	β_{max}	$P_{harv}(\omega)$	$P_{harv}\|_{\omega=\omega_c}$	P_{lim}
M	=	=	=	↗	↗	↗
x_0	↗	↘	=	↗	=	=
ω_0	↘	=*	↗	=	=*	↘
R	=	∿	∿	∿	∿	=
k_m^2	=	↘	↗	↗	∿	=
Q	=	↗	↗	=	↗	↗
γ_m	=	↗	=	=	↗	↗

Table 5 as well as the analysis of this section allow to get an intuitive understanding of the influences of each parameter on the characteristics of the bistable energy harvester. For example, in order to increase the cut-off frequency of the interwell motion, Table 5 shows that either the quality factor or the acceleration amplitude can be increased. Decreasing the stable position x_0 or the electromechanical coupling k_m^2 also leads to an increase of the cut-off frequency. Finally, the load resistance can also be adjusted in order to tune the cut-off frequency, even though the impact of R on ω_c is not monotonic (Fig.14.a). Note that the influence of the electrical time constant (defined as $\tau_e = RC_p$ [40, 41]) is the same as the influence of the resistance R. As shown in Fig.14, there exists an optimal electrical time constant that maximizes the harvested power. If τ_e deviates from this value, the harvested power decreases.

Table 5 is valid for bistable VEH whose voltage influence on the resonator dynamics is nonlinear (Fig.8). For bistable VEH whose voltage influence on the resonator dynamics is linear (Fig.7), the influences are slightly different because β does not depend on (x_m/x_0) (24). Table 6 summarizes theses influences.

Conclusion

Due to their complex dynamics, bistable vibration energy harvesters are usually studied with numerical simulations or semi-analytical models. In this study, closed-form expressions of the displacement amplitude, harvested power, and cut-off frequency of bistable VEH have been been derived. These simple analytical expressions are in good agreement with both numerical simulations and experimental results obtained on a bistable PEH. The proposed models allow to understand and predict the influences of each parameter of bistable energy harvesters on their power-frequency response. As a matter of exemple, these models allow to predict the influences of the mechanical quality factor, inertial mass, and electromechanical coupling on the cut-off frequency of the interwell motion and on the power-frequency response of any bistable VEH.

Such closed-form models might help scientists in finding the best trade-off while sizing a bistable energy harvester for any applicative cases. They might also help in developping an intuitive understanding of the intricate dynamics of bistable energy harvesters. Although in the present study, the analytical models have been derived for a resistive load, future works will focus on extending these models in order to predict the power-frequency response of bistable VEH connected to nonlinear electrical interfaces.

Acknowledgments

The authors wish to thanks N. Bencheikh and T. Payre from Cedrat Technologies for their contribution in the design of the prototype of the bistable vibration energy harvester.

This project has received funding from the European Union's Horizon 2020 research and innovation program under grant agreement No 862289.

References

[1] M. V. Tholl *et al.*, « Subdermal solar energy harvesting – A new way to power autonomous electric implants », *Applied Energy*, vol. 269, p. 114948, 2020, doi: 10.1016/j.apenergy.2020.114948.
[2] M. Lallart *et al.*, « Heusler alloy-based heat engine using pyroelectric conversion for small-scale thermal energy harvesting », *Applied Energy*, vol. 288, p. 116617, 2021, doi: 10.1016/j.apenergy.2021.116617.
[3] C. Wei and X. Jing, « A comprehensive review on vibration energy harvesting: Modelling and realization », *Renewable and Sustainable Energy Reviews*, vol. 74, p. 1-18, 2017, doi: 10.1016/j.rser.2017.01.073.
[4] X. Gu, S. Hemour, and K. Wu, « Far-Field Wireless Power Harvesting: Nonlinear Modeling, Rectenna Design, and Emerging Applications », *Proceedings of the IEEE*, vol. 110, nº 1, p. 56-73, 2022, doi: 10.1109/JPROC.2021.3127930.
[5] J. Siang, M. h. Lim, and M. Salman Leong, « Review of vibration-based energy harvesting technology: Mechanism and architectural approach », *International Journal of Energy Research*, vol. 42, nº 5, p. 1866-1893, 2018, doi: 10.1002/er.3986.
[6] A. Morel, A. Badel, Y. Wanderoild, and G. Pillonnet, « A unified N-SECE strategy for highly coupled piezoelectric energy scavengers », *Smart Mater. Struct.*, vol. 27, nº 8, p. 084002, 2018, doi: 10.1088/1361-665X/aac3b6.
[7] A. Morel *et al.*, « A comparative study of electrical interfaces for tunable piezoelectric vibration energy harvesting », *Smart Mater. Struct.*, vol. 31, nº 4, p. 045016, 2022, doi: 10.1088/1361-665X/ac54e8.
[8] S. P. Pellegrini, N. Tolou, M. Schenk, and J. L. Herder, « Bistable vibration energy harvesters: A review », *Journal of Intelligent Material Systems and Structures*, vol. 24, nº 11, p. 1303-1312, 2013, doi: 10.1177/1045389X12444940.
[9] B. P. Mann and B. A. Owens, « Investigations of a nonlinear energy harvester with a bistable potential well », *Journal of Sound and Vibration*, vol. 329, nº 9, p. 1215-1226, 2010, doi: 10.1016/j.jsv.2009.11.034.
[10] A. Syta, G. Litak, M. I. Friswell, and S. Adhikari, « Multiple solutions and corresponding power output of a nonlinear bistable piezoelectric energy harvester », *Eur. Phys. J. B*, vol. 89, nº 4, p. 99, 2016, doi: 10.1140/epjb/e2016-60699-0.
[11] T. Huguet *et al.*, « Drastic bandwidth enhancement of bistable energy harvesters: study of subharmonic behaviors and their stability robustness », *Applied Energy*, vol. 226, p. 607-617, 2020, doi: 10.1016/j.apenergy.2018.06.011.
[12] L. Chen *et al.*, « A numerical-experimental dynamics analysis of high-efficiency and broadband bistable energy harvester with self-decreasing potential barrier effect », *Applied Energy*, vol. 317, p. 119161, 2022, doi: 10.1016/j.apenergy.2022.119161.
[13] S. M. Shahruz, « Increasing the Efficiency of Energy Scavengers by Magnets », *Journal of Computational and Nonlinear Dynamics*, vol. 3, nº 4, 2008, doi: 10.1115/1.2960486.
[14] C. R. McInnes, D. G. Gorman, and M. P. Cartmell, « Enhanced vibrational energy harvesting using nonlinear stochastic resonance », *Journal of Sound and Vibration*, vol. 318, nº 4, p. 655-662, 2008, doi: 10.1016/j.jsv.2008.07.017.
[15] F. Cottone, H. Vocca, and L. Gammaitoni, « Nonlinear Energy Harvesting », *Phys. Rev. Lett.*, vol. 102, nº 8, p. 080601, 2009, doi: 10.1103/PhysRevLett.102.080601.
[16] H. Vocca *et al.*, « Kinetic energy harvesting with bistable oscillators », *Applied Energy*, vol. 97, p. 771-776, 2012, doi: 10.1016/j.apenergy.2011.12.087.
[17] A. Erturk, J. Hoffmann, and D. J. Inman, « A piezomagnetoelastic structure for broadband vibration energy harvesting », *Appl. Phys. Lett.*, vol. 94, nº 25, p. 254102, 2009, doi: 10.1063/1.3159815.
[18] A. Erturk and D. J. Inman, « Broadband piezoelectric power generation on high-energy orbits of the bistable Duffing oscillator with electromechanical coupling », *Journal of Sound and Vibration*, vol. 330, nº 10, p. 2339-2353, 2011, doi: 10.1016/j.jsv.2010.11.018.
[19] A. J. Sneller, P. Cette, and B. P. Mann, « Experimental investigation of a post-buckled piezoelectric beam with an attached central mass used to harvest energy », *Proceedings of the Institution of Mechanical Engineers, Part I: Journal of Systems and Control Engineering*, vol. 225, nº 4, p. 497-509, 2011, doi: 10.1177/0959651811401954.
[20] S. C. Stanton, B. A. M. Owens, and B. P. Mann, « Harmonic balance analysis of the bistable piezoelectric inertial generator », *Journal of Sound and Vibration*, vol. 331, nº 15, p. 3617-3627, 2012, doi: 10.1016/j.jsv.2012.03.012.
[21] M. Panyam, R. Masana, and M. F. Daqaq, « On approximating the effective bandwidth of bi-stable energy harvesters », *International Journal of Non-Linear Mechanics*, vol. 67, p. 153-163, 2014, doi: 10.1016/j.ijnonlinmec.2014.09.002.
[22] W. Liu, F. Formosa, A. Badel, "Optimization study of a piezoelectric bistable generator with doubled voltage frequency using harmonic balance method", *Journal of Intelligent Material Systems and Structures*, vol. 28, n°5, p. 671-686, 2017.
[23] T. Huguet, A. Badel, et M. Lallart, « Parametric analysis for optimized piezoelectric bistable vibration energy harvesters », *Smart Mater. Struct.*, vol. 28, nº 11, p. 115009, 2019, doi: 10.1088/1361-665X/ab45c6.
[24] A. Morel, A. Badel, R. Grézaud, P. Gasnier, G. Despesse, and G. Pillonnet, « Resistive and reactive loads' influences on highly coupled piezoelectric generators for wideband vibrations energy harvesting », *Journal of Intelligent Material Systems and Structures*, vol. 30, nº 3, p. 386-399, 2019, doi: 10.1177/1045389X18810802.
[25] C. Lan, Y. Liao, G. Hu, and L. Tang, « Equivalent impedance and power analysis of monostable piezoelectric energy harvesters », *Journal of Intelligent Material Systems and Structures*, vol. 31, nº 14, p. 1697-1715, 2020, doi: 10.1177/1045389X20930080.
[26] G. Sebald, H. Kuwano, D. Guyomar, and B. Ducharne, "Simulation of a Duffing oscillator for broadband energy harvesting", *Smart Mater. Struct.*, vol. 20, p. 075022, 2011.
[27] C. Saint-Martin et al., "Power expectation as a unified metric for the evaluation of vibration energy harvesters", *Mechanical Systems and Signal Processing*, vol. 181, p. 109482, 2022.
[28] V.G. Cleante, M.J. Brennan, G. Gatti, D.J. Thompson, "On the target frequency for harvesting energy from track vibrations due to passing trains", *Mechanical Systems and Signal Processing*, vol. 114, p. 212-223, 2019.
[29] S. Hanly, "Vibration analysis: FFT, PSD, and Spectrogram Basics", 2016.
[30] N. Cohen, I. Bucher, M. Feldman, "Slow-fast response decomposition of a bi-stable energy harvester", *Mechanical Systems and Signal Processing*, vol. 31, p. 29-39, 2012.

[31] W. Q. Liu, A. Badel, F. Formosa, Y. P. Wu, and A. Agbossou, « Novel piezoelectric bistable oscillator architecture for wideband vibration energy harvesting », *Smart Mater. Struct.*, vol. 22, nº 3, p. 035013, 2013, doi: 10.1088/0964-1726/22/3/035013.
[32] R. L. Harne, M. Thota, and K. W. Wang, « Concise and high-fidelity predictive criteria for maximizing performance and robustness of bistable energy harvesters », *Appl. Phys. Lett.*, vol. 102, nº 5, p. 053903, 2013, doi: 10.1063/1.4790381.
[33] Y. Liao and H. Sodano, « Optimal power, power limit and damping of vibration based piezoelectric power harvesters », *Smart Mater. Struct.*, vol. 27, nº 7, p. 075057, 2018, doi: 10.1088/1361-665X/aabf4a.
[34] A. Morel *et al.*, « 32.2 Self-Tunable Phase-Shifted SECE Piezoelectric Energy-Harvesting IC with a 30nW MPPT Achieving 446% Energy-Bandwidth Improvement and 94% Efficiency », in *2020 IEEE International Solid- State Circuits Conference - (ISSCC)*, 2020, p. 488-490. doi: 10.1109/ISSCC19947.2020.9062972.
[35] H. Xia, Y. Xia, Y. Ye, L. Qian, G. Shi, and R. Chen, « Analysis and Simulation of Synchronous Electric Charge Partial Extraction Technique for Efficient Piezoelectric Energy Harvesting », *IEEE Sensors Journal*, vol. 18, nº 15, p. 6235-6244, 2018, doi: 10.1109/JSEN.2018.2846256.
[36] E. Arroyo, A. Badel, F. Formosa, Y. Wu, and J. Qiu, « Comparison of electromagnetic and piezoelectric vibration energy harvesters: Model and experiments », *Sensors and Actuators A: Physical*, vol. 183, p. 148-156, 2012, doi: 10.1016/j.sna.2012.04.033.
[37] Y. Liao and H. A. Sodano, « Model of a single mode energy harvester and properties for optimal power generation », *Smart Mater. Struct.*, vol. 17, nº 6, p. 065026, 2008, doi: 10.1088/0964-1726/17/6/065026.
[38] B. Ando, S. Baglio, A.R. Bulsara, and V. Marletta, « A bistable buckled beam based approach for vibrational-energy harvesting », *Sensors and Actuators A: Physical*, vol. 211, p. 153-161, 2014, doi: 10.1016/j.sna.2013.12.027
[39] Y. C. Shu and I. C. Lien, « Analysis of power output for piezoelectric energy harvesting systems », *Smart Mater. Struct.*, vol. 15, nº 6, p. 1499-1512, 2006, doi: 10.1088/0964-1726/15/6/001.
[40] M. F. Daqaq, "On intentional introduction of stiffness nonlinearities for energy harvesting under white Gaussian excitations", *Nonlinear Dynamics*, vol. 69, n°3, p. 1063–1079, 2012, doi:10.1007/s11071-012-0327-0.
[41] S. S. Dasgupta, V. Rajamohan, A. K. Jha, "Dynamic Characterization of a bistable energy harvester under gaussian white noise for larger time constant", *Arabian Journal for Science and Engineering*, vol.44, n°2, p. 721-730, 2018, doi:10.1007/s13369-018-3187-1.

Appendix A – Proof of $\psi = \pi/2$ condition for the interwell motion cut-off frequency

The mechanical power in the harvester coming from the vibration can expressed as (33):

$$P_{vib} = \frac{1}{T}\int_0^T M\,\gamma(t)\,\dot{x}(t)dt \tag{33}$$

Solving (33) with the first-harmonic assumptions ($x(t) = x_m \cos(\omega t), \gamma(t) = \gamma_m cos(\omega t + \psi)$) yields (34):

$$P_{vib} = \frac{M\,\gamma_m\,x_m\,\omega\,\sin(\psi)}{2} \tag{34}$$

On the other hand, the power dissipated in the mechanical damper μ_m and electrical damper μ_e can be expressed as:

$$P_{diss} = \frac{1}{T}\int_0^T (\mu_m + \mu_e)\,\dot{x}^2(t)\,dt \tag{35}$$

Solving the integral in (35), the expression of the power dissipated in the dampers becomes (36):

$$P_{diss} = \frac{\omega^2 x_m^2\,(\mu_m + \mu_e)}{2} \tag{36}$$

Because of energy conservation, the power dissipated in the dampers should be equal to the power coming from the mechanical vibration. Therefore, equation (37) is obtained:

$$\frac{\omega^2 x_m^2\,(\mu_m + \mu_e)}{2} = \frac{M\,\gamma_m\,x_m\omega\,\sin(\psi)}{2} \tag{37}$$

Re-arranging the terms in (37) and replacing x_m by its expression (14) yields (38):

$$\sin(\psi) = \frac{2}{\sqrt{3}}\frac{x_0\,\omega}{\gamma_m}\frac{(1+\beta)}{Q}\sqrt{1+\frac{2\omega^2}{\omega_0^2}} \tag{38}$$

(38) means that the phase-shift ψ between the displacement x and the excitation γ depends on the vibration frequency ω. If the vibration frequency is increased, P_{vib} grows because $\sin(\psi)$ gets larger with ω. The maximum value of P_{vib} is obtained when $\sin(\psi) = 1$, in other words when $\psi = \frac{\pi}{2}$, which corresponds to $\omega = \omega_c$. For larger frequencies, the condition (38) cannot be met (because $sin\,(\psi) \leq 1$), meaning that the interwell motion does not exist.

Appendix B - Details of the testing scenario set up in section 3

In this appendix, we provide details of the testing scenario that allow to obtain the experimental data of the present paper and to plot Fig.11-16.

As precised in section 3, Fig.11 was obtained for 600 frequencies between 30Hz and 90Hz and for 70 resistances from 100Ω to $30k\Omega$. For each of the 70 resistances, two frequency sweeps have been realized, in order to obtain a complete characterization of the bistable PEH interwell motion. The automated procedure that has been followed is described in Fig.22.

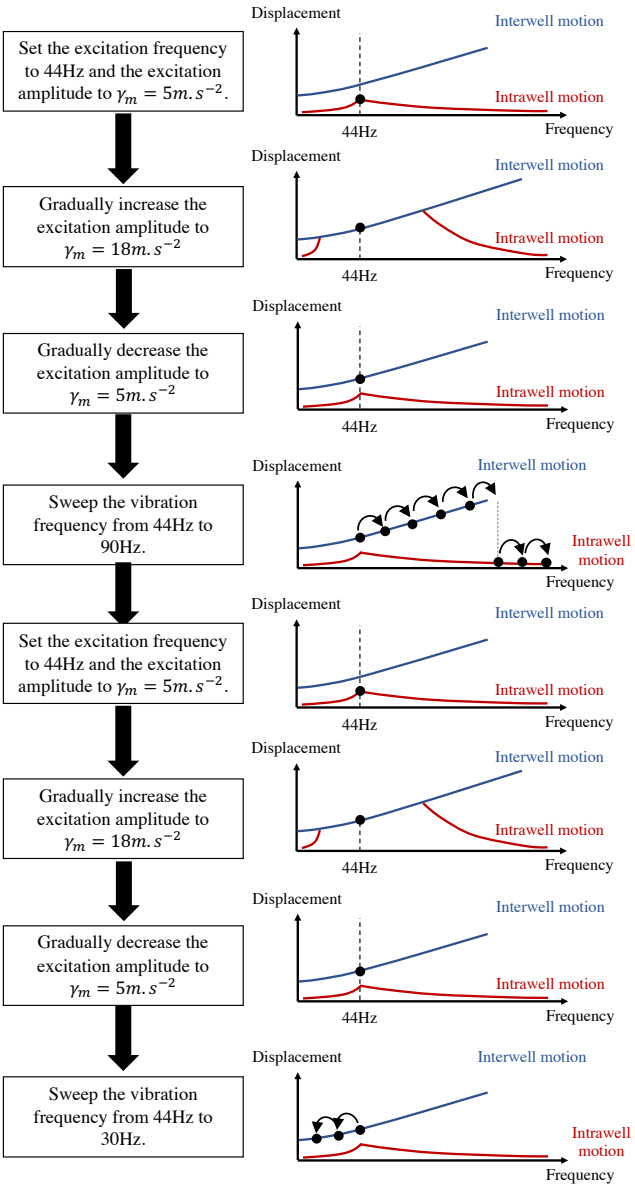

Figure 22. Procedure to characterize the interwell motion of the bistable PEH.

First, the excitation frequency is set to 44Hz[4], and the PEH operates in intrawell orbits. Thereafter, the acceleration amplitude is gradually increased, up to 18m.s^{-2}, in order to jump to the interwell orbits of the PEH. Then, the acceleration amplitude is decreased back to 5m.s^{-2}. The decrease of the acceleration is done slowly, in 100 seconds, in order to maintain the interwell motion even though the acceleration amplitude is reduced. Finally, the frequency has been swept up to 90Hz (and swept down to 30Hz), in order to characterize the interwell motion as a function of the vibration frequency. For 600 frequencies between 30Hz and 90Hz, the voltage, displacement, speed, and acceleration have been acquired during 500 periods.

As illustrated in Fig.23, the same procedure has been repeated for 70 values of resistance connected to the PEH. For each of the 63000 combinations of frequency and resistance, the data have been acquired, which allowed to plot Fig.11-14. Note that the same procedure has been followed to plot Fig.15-16, except that 20 accelerations have been tested instead of 70 resistances.

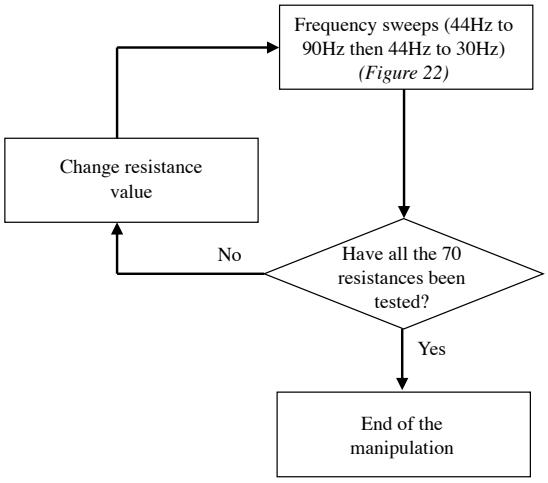

Figure 23. Flowchart illustrating the steps to obtain the data shown in Fig.11-14.

[4] This particular frequency has been selected because, with our PEH, the interwell motion is most easily obtained at 44Hz.